A piston and tilt wavefront sensor dedicated to the cophasing of segmented optics in low light level conditions

Thomas Rousseaux, Jérôme Primot, Julien Jaeck, Bastien Rouzé, Cécile Le Gall, Cindy Bellanger

Optics and Lasers in Engineering 181 (2024) 108412

Contents lists available at ScienceDirect

Optics and Lasers in Engineering

journal homepage: www.elsevier.com/locate/optlaseng

A piston and tilt wavefront sensor dedicated to the cophasing of segmented optics in low light level conditions

Thomas Rousseaux *, Jérôme Primot, Julien Jaeck, Bastien Rouzé, Cécile Le Gall, Cindy Bellanger *

DOTA, ONERA, Université Paris-Saclay, 91120, Palaiseau, France

ARTICLE INFO

Keywords:
Pistil interferometry
Multiple-wave lateral shearing interferometry
Mirrors co-phasing
Wavefront sensing
Telescope

ABSTRACT

We present a new interferometer to measure piston, tip and tilt of segmented mirrors, using the combination of an optical grating and a microlens array. Since this interferometer is able to collect all the incident light and to operate with a large spectra bandwidth, it is particularly suitable to operate in low light level conditions, for example for the co-phasing of segmented primary mirrors like James Webb Space Telescope. We tested our new device on a 37-segment deformable mirror and obtained an accuracy better than $\lambda/100$. The measurement is self-referenced and errors can be estimated on the measurement itself thanks to closure relationships.

1. Introduction

Regular segmented surfaces can be found in a wide range of industrial and research applications, from MOEMS components widely used in industry, to coherent beam combining lasers (CBC) [1–3] and space telescopes [4–7]. Whatever the application, their use requires perfect control of the relative height between the different segments to within a few fractions of a wavelength. We approached this question through the problem of CBC lasers. The principle is the cooperation by far-field constructive interference of laser beams placed in a regular, compact mesh. One way of achieving such interference is to collectively measure the phase of each of the near-field beams and then apply the appropriate feedback on the lasers in the system. Measurement then amounts to evaluating the phase of a regular segmented wavefront made up of a juxtaposition of individual plane waves, affected by differential pistons and tilts. To this end, we have developed Pistil (PISton and TILt) interferometry [8–10], the basic principle of which is simply to make each pair of unit beams on the wave surface to interfere, in order to evaluate their relative phase differences. The results we presented, using real lasers or segmented mirrors for laboratory validation, showed phase measurement accuracy better than $\lambda/100$.

The astronomical community reacted to the publication of our papers, considering this kind of technique could be adapted to the cophasing of large segmented space mirrors such as JWST or LUVOIR [11,6,12–17]. This type of application imposes an additional constraint that does not exist in the world of power lasers: low-light-level operation. Pistil as such was not very suitable, as it has a relatively low light efficiency. We therefore improved the device to make it more effective. This new version is the scope of the present publication.

In the first section, we will describe the set-up, with a focus on preserving the light efficiency. We will then introduce the theoretical description of the interferograms produced. Reasoning about chromaticity will show that this device can support large spectral bandwidths, reinforcing its ability to operate in low-light conditions. We also present the associated treatment to recover the relative pistons and tilts between the segments. A specific section will be devoted to its ability to simultaneously evaluate the noise on the reconstruction with the measure itself, based on closure relationships. In the last section, an experiment is conducted using a segmented mirror well known to the astronomical community, the IRIS-AO PT-111.

2. Principle of the Full Light Pistil Interferometer

The fundamental principle of Pistil interferometry has been retained in this new evolution of the analyzer (Fig. 1). The phase of each segment of the wavefront, considered as a plane wave only affected with tip, tilt and piston, is compared with its six direct neighbors. To do so, the total segmented wavefront is imaged on the analyzer, which consists of a microlens array (MLA) and a diffraction grating joined together in a single component. For sake of clarity, basic principle is presented in one dimension with only two segments. The MLA acts as a beam concentrator (Fig. 1, Left). It reduces the diameter of each beam by a factor of 2 at a

* Corresponding authors.
E-mail addresses: thomas.rousseaux@onera.fr (T. Rousseaux), cindy.bellanger@onera.fr (C. Bellanger).

https://doi.org/10.1016/j.optlaseng.2024.108412
Received 21 March 2024; Received in revised form 3 June 2024; Accepted 27 June 2024
Available online 14 July 2024

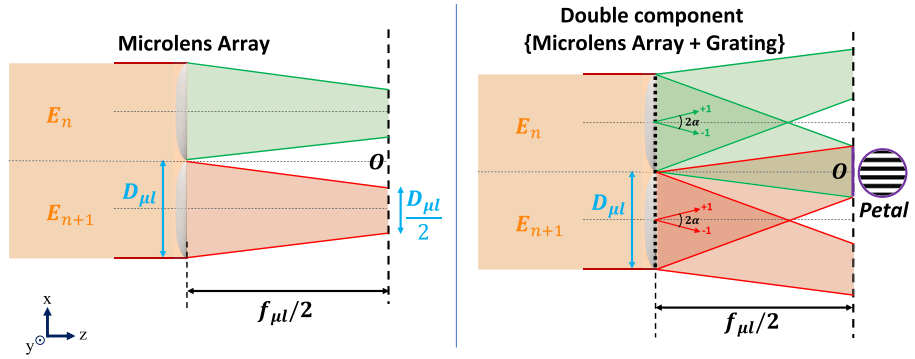

Fig. 1. Observation at $f_{\mu l}/2$ - Left: Propagation of two contiguous segments of the analyzed wavefront through the microlens array - Right: Propagation of the wavefront through the complete Full Light Pistil component {MLA + grating}.

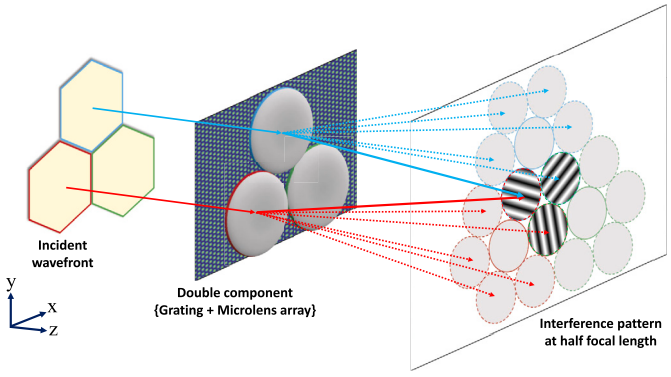

Fig. 2. Basic principle of Full Light Pistil Interferometry for a hexagonal patterned segmented beam.

distance of half a focal length. A diffraction grating is joined on it to produce lateral shifted replicas of the segmented wavefront on its +1 and -1 diffraction orders, so as to create only two-wave interference areas between beams from neighboring segments (Fig. 1, Right). Hereafter, we will refer as "Petal" these two-waves interference areas. Piston difference between segments translates into fringe translation, tip and tilt difference change respectively orientation and frequency of the fringes in the impinging petal.

The diffraction grating is optimized to diffract only the +1 and -1 diffraction orders, with a given angle α according to the grating formula in the small angle approximation ($\alpha \ll 1$):

$$\alpha = \frac{\lambda_0}{P_g} \tag{1}$$

Where λ_0 is the wavelength and P_g the grating pitch. Higher orders are canceled or attenuated as much as possible. By geometric considerations (see Fig. 1), we can also easily assume that:

$$\alpha = \frac{D_{\mu l}}{f_{\mu l}} \tag{2}$$

Where $f_{\mu l}$ is the focal lens of the MLA and $D_{\mu l}$ the diameter of a microlens. The two components {MLA + grating} must then be tuned according to the following relationship:

$$P_g = \frac{\lambda_0}{\alpha} = \frac{f_{\mu l}\lambda_0}{D_{\mu l}} \tag{3}$$

If we generalize, on a hexagonal two-dimensional incident wavefront, the principle of Full Light Pistil is replicated along the three main axes of the pattern. It can be summed up as described in Fig. 2. The resulting interferogram is then analyzed to quantify the phase relationships between the segments collectively, accurately and robustly. An example of analysis procedure is explained in Part 6.

It should be noted that MLA can be used in a different configuration, after their focal plane, while retaining their function as beam concentrator, as described in Fig. 3. For the same grating pitch P_g, the diffraction angle α remains the same, so the new focal length $f'_{\mu l}$ of the MLA is then divided by three with respect to previous $f_{\mu l}$, so that interference appears at $3f'_{\mu l}/2$. This configuration may be of interest in facilitating technological choices or in adapting on supplier availability.

3. Theoretical modeling

The aim of this section is to propose a model of the fringe pattern formed in the Petal created by the interference of replicas of two neighboring surface elements n and $n+1$ (red and green in Fig. 1). The model is written for the configuration with observation at $f_{\mu l}/2$. It can easily be transposed for the configuration with observation at $3f'_{\mu l}/2$. Each has a given phase $Seg_k(x,y)$. This phase is constituted of a piston P_k, a tip tip_k, a tilt $tilt_k$, and a residual mirror aberration $\Phi_k(x,y)$, independent of the wavelength (polishing error, ...).

$$Seg_k(x,y) = P_k + y \cdot tip_k + x \cdot tilt_k + \Phi_k(x,y) \qquad k = n \text{ or } (n+1) \tag{4}$$

The set-up is assumed to be optimized for the wavelength λ_0, central wavelength of the spectral bandwidth $[\lambda_0 - \Delta\lambda_0, \lambda_0 + \Delta\lambda_0]$. The origin O is placed at the center of the petal (see Fig. 1 and Fig. 3). We can then write the complex fields $E_{n,-1}(x,y,\Delta\lambda)$ and $E_{n+1,+1}(x,y,\Delta\lambda)$, referenced with index +1 or -1, depending on whether the replica comes from a +1 or -1 diffraction order, where $\Delta\lambda$ is the deviation from the central wavelength λ_0; EO_n and EO_{n+1} are the amplitudes of the fields, considered as a constant for the sake of simplicity. $E_{n,-1}(x,y,\Delta\lambda)$ and $E_{n+1,+1}(x,y,\Delta\lambda)$ are affected by their phase $Seg_n(x,y)$ and $Seg_{n+1}(x,y)$ (first exponential term), that propagate through the grating (second exponential term) and MLA (third exponential term), until the observation plane at $f_{\mu l}/2$:

$$E_{n,-1}(x,y,\Delta\lambda) = EO_n e^{\frac{2i\pi}{\lambda_0+\Delta\lambda}Seg_n(x,y)} e^{-i\left(-\frac{2\pi}{P_g}x\right)} e^{\frac{2i\pi\left(\left(x-s_x^{\Delta\lambda}\right)^2+y^2\right)}{(\lambda_0+\Delta\lambda)f_{\mu l}}} \times Disk\left(x - s_x^{\Delta\lambda}, y\right) \tag{5}$$

$$E_{n+1,+1}(x,y,\Delta\lambda) = EO_{n+1} e^{\frac{2i\pi}{\lambda_0+\Delta\lambda}Seg_{n+1}(x,y)} e^{-i\left(+\frac{2\pi}{P_g}x\right)} e^{\frac{2i\pi\left(\left(x+s_x^{\Delta\lambda}\right)^2+y^2\right)}{(\lambda_0+\Delta\lambda)f_{\mu l}}} \times Disk\left(x + s_x^{\Delta\lambda}, y\right) \tag{6}$$

In this expression, $Disk(x,y)$ is the amplitude support in the observation plane, with a diameter of $D_{\mu l}/2$, and $s_x^{\Delta\lambda}$ is the chromatic differential lateral shift of the replicas (see Fig. 4), defined as follows:

$$s_x^{\Delta\lambda} = \frac{\Delta\lambda f_{\mu l}}{2P_g} \tag{7}$$

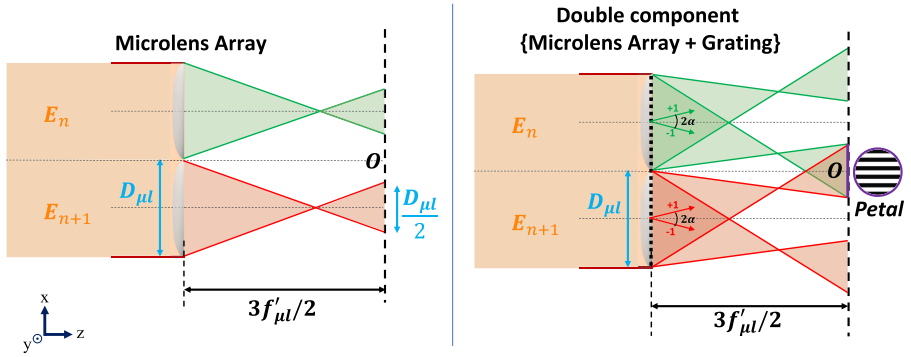

Fig. 3. Observation at $3f'_{\mu l}/2$ - Left: Propagation of two contiguous segments of the analyzed wavefront through the MLA - Right: Propagation of the wavefront through the complete Full Light Pistil component {MLA + grating}.

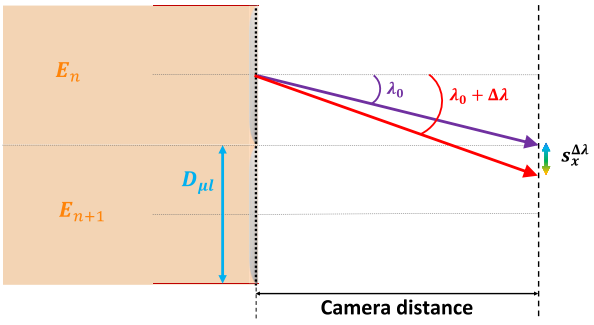

Fig. 4. Chromatic differential lateral shift $s_x^{\Delta\lambda}$ at observation plane $f_{\mu l}/2$ or $3f'_{\mu l}/2$.

The grating exponential term corresponds to the tilt introduced by the phase grating (-1 or +1 order) and is independent of the wavelength, as with all grating interferometers [18]. The MLA exponential term corresponds to its spherical wave considered in the $f_{\mu l}/2$ plane; notice that the center of this spherical wave depends on the wavelength.

Assuming that the spectral bandwidth $\Delta\lambda_0$ is small with respect to the central wavelength λ_0, we can write:

$$\frac{1}{\lambda_0 + \Delta\lambda} \approx \frac{1}{\lambda_0}\left(1 - \frac{\Delta\lambda}{\lambda_0}\right) \tag{8}$$

In the petal, the intensity of fringes is equal to:

$$\begin{aligned} I_{n,n+1}(x,y,\Delta\lambda) &= \left|E_{n,-1}(x,y,\Delta\lambda) + E_{n+1,+1}(x,y,\Delta\lambda)\right|^2 \\ &= 2I0_{n,n+1}\left(1 + \cos\left(2\pi\left(1 - \frac{\Delta\lambda}{\lambda_0}\right)\left(\frac{2x}{P_g} + \frac{\Delta Seg_{n,n+1}(x,y)}{\lambda_0}\right)\right)\right) \end{aligned} \tag{9}$$

With $I0_{n,n+1} = E0_n E0_{n+1}$ and

$$\Delta Seg_{n,n+1}(x,y) = Seg_n(x,y) - Seg_{n+1}(x,y) \tag{10}$$

To illustrate this formula, consider first that the two considered segments are only affected by piston terms. $\Delta Seg_{n,n+1}(x,y)$ is a constant, equal to the differential piston $\Delta P_{n,n+1} = (P_n - P_{n+1})$. This results in a x-translation of the fringes proportional to $\Delta P_{n,n+1}$. If this time we have only a tip, or respectively a tilt, for the two neighboring segments, we obtain respectively a rotation or a frequency change of the fringes. So, main defects of the non-cophase mirror are easily separated as they act differently on the fringe pattern. This property is characteristics of Piston and Tilt interferometry.

4. Broadband robustness

The setup's ability to work in low-light conditions depends essentially on the robustness of the fringes with respect to a wide spectral band. The effect of a broadening of the spectral range can be evaluated

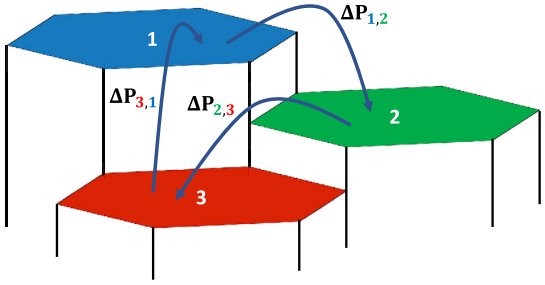

Fig. 5. Illustration of the closure relationships. The three arrows represent a path through that should verify $\Delta P_{1,2} + \Delta P_{2,3} + \Delta P_{3,1} = 0$ in ideal case.

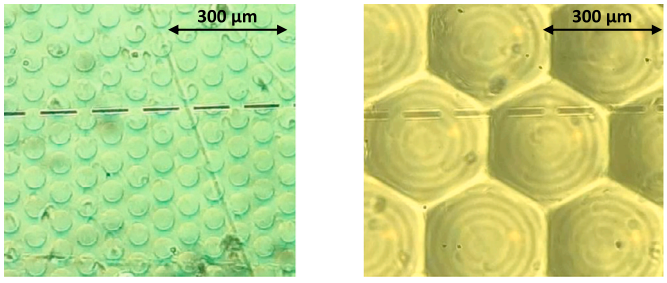

Fig. 6. Left: Picture of the phase grating - Right: Picture of the MLA.

by computing the integrated intensity $I_{int_{n,n+1}}(x,y)$, integrating Equation (9) with respect to $\Delta\lambda$ on spectral bandwidth:

$$\begin{aligned} I_{int_{n,n+1}}(x,y) = 2I0_{n,n+1}\int_{-\Delta\lambda_0}^{+\Delta\lambda_0} &\left(1 + \cos\left(2\pi\left(1 - \frac{\Delta\lambda}{\lambda_0}\right)\right.\right. \\ &\left.\left.\times\left(\frac{2x}{P_g} + \frac{\Delta Seg_{n,n+1}(x,y)}{\lambda_0}\right)\right)\right) d\Delta\lambda \end{aligned} \tag{11}$$

So:

$$\begin{aligned} I_{int_{n,n+1}}(x,y) = 2\Delta\lambda_0 I0_{n,n+1}&\left(1 + \cos\left(2\pi\left(\frac{2x}{P_g} + \frac{\Delta Seg_{n,n+1}(x,y)}{\lambda_0}\right)\right)\right. \\ &\left.\times \operatorname{sinc}\left(2\pi\Delta\lambda_0\left(\frac{x}{\lambda_0 P_g} + \frac{\Delta Seg_{n,n+1}(x,y)}{\lambda_0^2}\right)\right)\right) \end{aligned} \tag{12}$$

The fringes modulation is then only affected by a contrast term $C_{n,n+1}(x,y)$ related to the analyzed defect and expressed as follows:

$$C_{n,n+1}(x,y) = \operatorname{sinc}\left(2\pi\frac{\Delta\lambda_0}{\lambda_0}\left(\frac{x}{P_g} + \frac{\Delta Seg_{n,n+1}(x,y)}{\lambda_0}\right)\right) \tag{13}$$

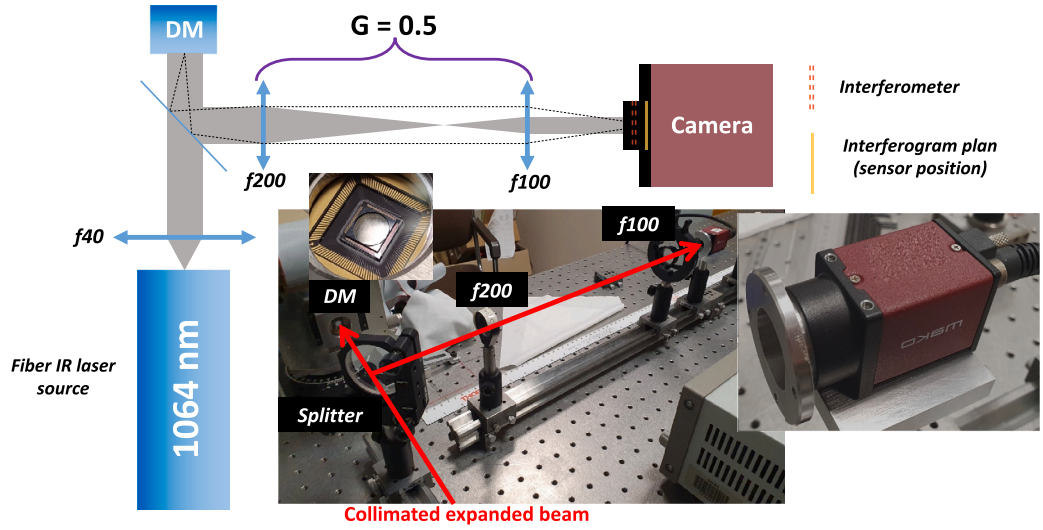

Fig. 7. Schematic diagram and picture of the experimental bench - Right: Picture of the Full Light Pistil Interferometer. The aluminum part in front of the camera contains the double component {MLA + grating}.

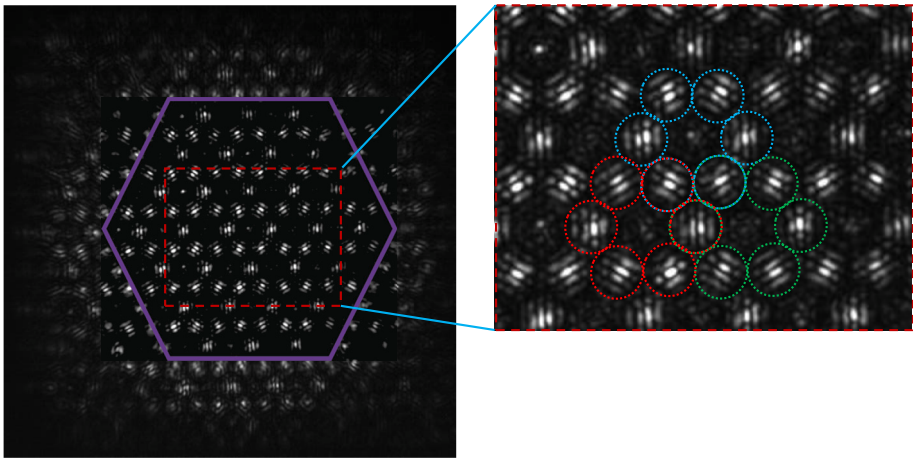

Fig. 8. Example of Pistil interferogram, in the purple hexagon. Doted colored circles are locations of petals, where replicas of two neighbors interfere (we used the same color code as in Fig. 2).

If we consider a practical case of four fringes per petal, which is a typical value used for Pistil interferometry to correctly evaluate both piston and tip/tilt, and the V band which central wavelength is $\lambda_0 = 550$ nm and spectral bandwidth is $2\Delta\lambda_0 = 89$ nm, we see that the maximum attenuation at the edge of the petal is approximately 9% for a differential piston of $\lambda_0/2$. This setup is therefore capable of supporting large spectral bandwidths without any major degradation in performance, which, combined with the close-to-one luminous efficiency obtained through the use of a MLA and a phase grating, argues in favor of low-light-level operation.

5. Error self-evaluation

As with all Pistil interferometers, we have an intrinsic property of error evaluation based on the measurement itself. For the sake of simplicity, we will consider here the case where only pistons are measured. Consider three segments numbered 1, 2 and 3, whose centers lie in an equilateral triangle (see Fig. 5). Pistil measures $\Delta P_{1,2}$, $\Delta P_{2,3}$ and $\Delta P_{3,1}$, three height differences for a closed path; so, by principle, the sum Err_{123} of these differential pistons should be zero. If it is not, this is due to the measurement error associated with each differential piston. Thus, considering all the segments by triangle, we can deduce many closure relationships. If we assume that the errors in the evaluation of differential pistons are independent, with a same variance $\sigma^2_{\Delta P}$, the variance of these closures relates directly to $\sigma^2_{\Delta P}$:

$$\sigma^2_{Err} = 3\sigma^2_{\Delta P} \tag{14}$$

6. Experimental validation

To test this technique experimentally, we built a prototype of a Full Light Pistil interferometer. For this first demonstration, we favored the use of off-the-shelf components, which led us to prefer the $3f'_{\mu l}/2$ configuration. Our device is then composed of a fused silica phase grating comprising two etching levels whose 51.1 μm diameter dots are 1165 nm deep with a 73 μm pitch, juxtaposed with a 300 μm pitch hexagonal patterned of 6 mm focal length MLA (see Fig. 6). The etching precision of the grating minimizes parasitic orders that can degrade fringe quality. The device has been inserted with a homemade mechanical mount into a commercial 1280 x 1024 non filtered Si visible camera with a pixel size of 5.3 μm^2.

We demonstrate on a segmented wavefront, realized with an expanded 1064 nm CW fiber laser diode that illuminates a 37-segment deformable mirror (DM) IRIS AO PTT-111 [19–21]. The setup is described in Fig. 7. Each segment can be controlled individually on demand in piston, tip and tilt. However, for this first demonstration, we

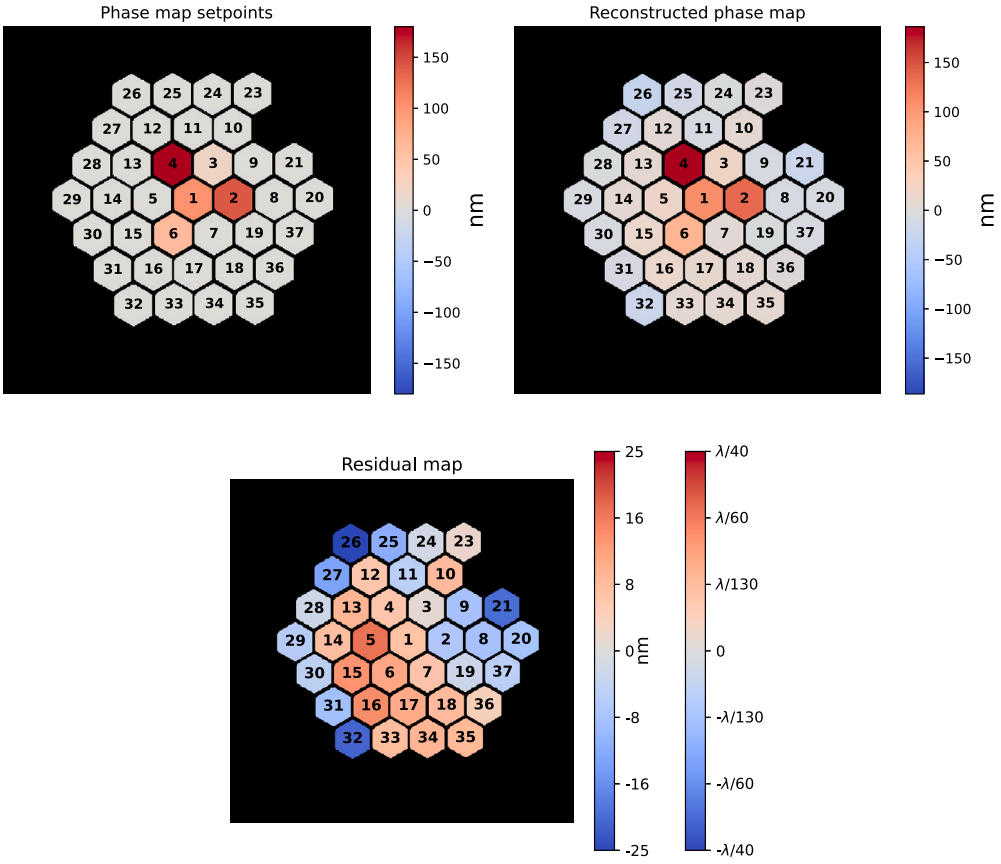

Fig. 9. Left: Phase map setpoint of the 36 segments of the mirror – Right: Reconstructed map – Bottom: Residual phase map, including command and measurement errors.

will only consider a piston control. An optimal system would require a camera with good quantum efficiency at 1 μm, but the quantum efficiency remains sufficient at 1064 nm for the concept proof.

The experimental interferogram is shown in Fig. 8. The six replicas issuing from three sub-beams have been surrounded by colored dotted lines, with the same convention color as in Fig. 2. Notice that the fringes outside the purple hexagon are not part of the interferogram, as they result from stray reflections on the reflective outer part of the considered segmented mirror. We can see hot spots due to diffraction from the edges of the microlenses, whose location on fringes is independent of the phase. They do not seem to have a major impact on the reconstruction.

This interferogram can be analyzed by a Fourier transform method [22,23], or by fringe correlation [24]. Then, using fringe movement analysis, the whole segmented surface can be reconstructed by integration of those measurements, with the Moore-Penrose least-squares method [25,26]. As there are more differential piston relationships than pistons to rebuild, measure is redundant. For example, we have 3 times 30 differences of pistons for a mirror made of 37 segments. This redundancy significantly increases the signal-to-noise ratio [8,27]. Furthermore, as the measurement is 2π-ambiguous, we can only measure pistons in the range $[-\lambda/2, \lambda/2]$. However, a two-color method allows to gain in measurement dynamics by using the Vernier effect, which gives an equivalent wavelength, as described in [19].

The light utilization depends on many parameters, such as the proportion of light ending up in the useful orders of the grating, the transmittance of the lenses and grating, or the quantum efficiency of the camera at the wavelength of study. The components have already been transmission-optimized for low light levels.

Fig. 9 shows respectively the command, the reconstructed and the residual phase maps. Residual phase map covers both mirror response errors and analyzer errors. Using closure relationships presented in Part 5 and shown in Fig. 10, we evaluate a precision of 6 nm RMS, better than $\lambda/100$. The largest residual concerns the element 5, which is closed to the element 4, corresponding to the strongest command, highlighting a cross-talk problem with this type of mirror, known elsewhere [19].

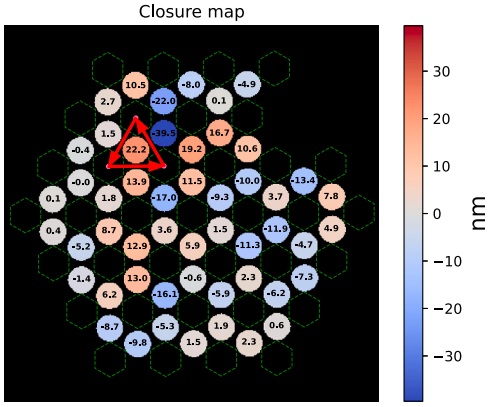

Fig. 10. 51 calculated closure relationships form the measurement of 3×30 differences of piston. Here, we only have 51 relationships due to the faulty segment of our segmented mirror. Green doted hexagons represent central areas from mirror segments. The standard deviation of this set of values is equal to $\sqrt{3}$ the standard deviation of pistons.

7. Conclusion

To take account of low-light level requirements, we have upgraded the Pistil device, originally developed for laser analysis for coherent combining purpose. The combined use of a microlens array and a grating

has enabled us to utilize all impinging photons, over a relatively wide spectral band while retaining the simplicity of a classic Pistil treatment. The ability to assess measurement accuracy from the measurement itself seems to us to be of great benefit. We are currently considering extending its use to astronomical observation, but this time at ground level, taking into account atmospheric turbulence contribution.

Funding

Investissements d'Avenir, Laboratoire d'excellence Physique Atomes Lumière Matière (ANR-10-LABX-0039-PALM).

CRediT authorship contribution statement

Thomas Rousseaux: Writing – original draft, Visualization, Software, Investigation, Formal analysis. **Jérôme Primot:** Writing – review & editing, Visualization, Supervision, Conceptualization. **Julien Jaeck:** Software, Formal analysis. **Bastien Rouzé:** Software, Formal analysis. **Cécile Le Gall:** Software, Formal analysis. **Cindy Bellanger:** Writing – review & editing, Visualization, Supervision, Conceptualization.

Declaration of competing interest

The authors declare the following financial interests/personal relationships which may be considered as potential competing interests: Thomas Rousseaux, Jerome Primot, Bastien Rouze, Julien Jaeck, Cindy Bellanger has patent #COMPOSANT OPTIQUE ET ANALYSEUR DE SURFACE D'ONDE COMPRENANT UN TEL COMPOSANT OPTIQUE (FR 22.13994) pending to ONERA (OFFICE NATIONAL D'ETUDES ET DE RECHERCHES AEROSPATIALES). Cindy Bellanger, Maxime Deprez, Laurent Lombard, Jerome Primot has patent #Wavefront sensor and method for determining differences in piston and tilt existing between several light beams (10175115) issued to ONERA (OFFICE NATIONAL D'ETUDES ET DE RECHERCHES AEROSPATIALES). If there are other authors, they declare that they have no known competing financial interests or personal relationships that could have appeared to influence the work reported in this paper.

Data availability

No data was used for the research described in the article.

Acknowledgements

We acknowledge Gilles Le Coadou and Éric Lambert for the design and the production of the support piece. We also acknowledge F. Zamkotsian from Laboratoire d'Astrophysique de Marseille and J-C. Chanteloup and I. Fsaifes from LULI, CNRS, École Polytchnique for fruitful discussions.

Appendix A. Supplementary material

Supplementary material related to this article can be found online at https://doi.org/10.1016/j.optlaseng.2024.108412.

References

[1] Chang H, Chang Q, Xi J, Hou T, Su R, Ma P, et al. First experimental demonstration of coherent beam combining of more than 100 beams. Photon Res 2020;8(12):1943. https://doi.org/10.1364/PRJ.409788. https://opg.optica.org/abstract.cfm?URI=prj-8-12-1943.

[2] Chang Q, Hou T, Long J, Deng Y, Chang H, Ma P, et al. Experimental phase stabilization of a 397-channel laser beam array via image processing in dynamic noise environment. J Lightwave Technol 2022:1–7. https://doi.org/10.1109/JLT.2022.3195822. https://ieeexplore.ieee.org/document/9847222/.

[3] Fsaifes I, Daniault L, Bellanger S, Veinhard M, Bourderionnet J, Larat C, et al. Coherent beam combining of 61 femtosecond fiber amplifiers. Opt Express 2020;28(14):20152. https://doi.org/10.1364/OE.394031. https://www.osapublishing.org/abstract.cfm?URI=oe-28-14-20152.

[4] Clampin M. The James webb space telescope (JWST). Adv Space Res 2008;41(12):1983–91. https://doi.org/10.1016/j.asr.2008.01.010. https://linkinghub.elsevier.com/retrieve/pii/S0273117708000410.

[5] Acton DS, Knight JS, Contos A, Grimaldi S, Terry J, Lightsey P, et al. Wavefront sensing and controls for the James webb space telescope. In: Clampin MC, Fazio GG, MacEwen HA, Oschmann JM, editors. Space telescopes and instrumentation 2012; 2012. p. 84422H. http://proceedings.spiedigitallibrary.org/proceeding.aspx?doi=10.1117/12.925015.

[6] Chanan G, Schoeck M, Troy M. Approach based on χ^2 to phasing segmented-mirror telescopes using multiple wavelengths: data reduction, wavelength selection, capture range. Appl Opt 2022;61(4):935. https://doi.org/10.1364/AO.447439. https://opg.optica.org/abstract.cfm?URI=ao-61-4-935.

[7] LUVOIR Team. The LUVOIR mission concept study final report. arXiv preprint. arXiv:1912.06219, 2019.

[8] Deprez M, Wattellier B, Bellanger C, Lombard L, Primot J. Phase measurement of a segmented wave front using PISton and TILt interferometry (PISTIL). Opt Express 2018;26(5):5212. https://doi.org/10.1364/OE.26.005212. https://www.osapublishing.org/abstract.cfm?URI=oe-26-5-5212.

[9] Rouzé B, Primot J, Zamkotsian F, Lanzoni P, Bellanger C. PISTIL interferometry: a modular, plug-and-play metrology mean for diagnosis of coherently combined laser arrays. In: Zervas MN, Jauregui-Misas C, editors. Fiber lasers XVIII: technology and systems, SPIE, online only, United States; 2021. p. 52. https://www.spiedigitallibrary.org/conference-proceedings-of-spie/11665/2582509/PISTIL-interferometry--a-modular-plug-and-play-metrology-mean/10.1117/12.2582509.full.

[10] Rouzé B. Interférométrie PISTIL pour le diagnostic de la combinaison cohérente de sources laser fibrées. Ph.D. thesis. Université Paris-Saclay; 2021.

[11] Xie Z, Lepine T, Houllier T, Ma H, Mourard D, Labeyrie A. Hypertelescope with multiplexed fields of view. Opt Lett 2020;45(7):1878. https://doi.org/10.1364/OL.385953. https://opg.optica.org/abstract.cfm?URI=ol-45-7-1878.

[12] Sato S, Mizutani T. Cross-fringe piston sensor for segmented optics. Appl Opt 2022;61(14):3972. https://doi.org/10.1364/AO.454425. https://opg.optica.org/abstract.cfm?URI=ao-61-14-3972.

[13] Qin R, Yin Z, Ke Y, Liu Y. Large piston error detection method based on the multiwavelength phase shift interference and dynamic adjustment strategy. Photonics 2022;9(10):694. https://doi.org/10.3390/photonics9100694. https://www.mdpi.com/2304-6732/9/10/694.

[14] Yang L, Yang D, Yang Z, Liu Z. Co-phase state detection for segmented mirrors by dual-wavelength optical vortex phase-shifting interferometry. Opt Express 2022;30(9):14088. https://doi.org/10.1364/OE.455890. https://opg.optica.org/abstract.cfm?URI=oe-30-9-14088.

[15] Schoeck M, Chanan G. Analysis of edge jumps in multi-wavelength phasing of segmented-mirror telescopes. Appl Opt 2023;62(25):6760. https://doi.org/10.1364/AO.499167. https://opg.optica.org/abstract.cfm?URI=ao-62-25-6760.

[16] Wilhelm R, Luong B, Courteville A, Estival S, Gonté F, Schuhler N. Dual-wavelength low-coherence instantaneous phase-shifting interferometer to measure the shape of a segmented mirror with subnanometer precision. Appl Opt 2008;47(29):5473. https://doi.org/10.1364/AO.47.005473. https://opg.optica.org/abstract.cfm?URI=ao-47-29-5473.

[17] Leveque S, Falldorf C, Klattenhoff R, Cheffot A. Day-time local phasing of neighbouring segments of the e-ELT primary mirror, based simultaneous multi-λ shearing interferometry. In: Navarro R, Burge JH, editors. Advances in optical and mechanical technologies for telescopes and instrumentation II; 2016. p. 99124G. http://proceedings.spiedigitallibrary.org/proceeding.aspx?doi=10.1117/12.2235241.

[18] Ronchi V. Forty years of history of a grating interferometer. Appl Opt 1964;3(4):437. https://doi.org/10.1364/AO.3.000437. https://opg.optica.org/abstract.cfm?URI=ao-3-4-437.

[19] Rouze B, Primot J, Lanzoni P, Zamkotsian F, Tache F, Bellanger C. High-dynamic range segmented mirror metrology by two-wavelength PISTIL interferometry: demonstration and performance. Opt Express 2020;28(22):32415. https://doi.org/10.1364/OE.398390. https://www.osapublishing.org/abstract.cfm?URI=oe-28-22-32415.

[20] Helmbrecht MA, He M, Kempf CJ, Marchis F. Long-term stability and temperature variability of Iris AO segmented MEMS deformable mirrors. In: Marchetti E, Close LM, Véran J-P, editors. Adaptive optics systems V; 2016. p. 990981. http://proceedings.spiedigitallibrary.org/proceeding.aspx?doi=10.1117/12.2233923.

[21] Zamkotsian F, Lanzoni P, Barette R, Helmbrecht M, Marchis F, Teichman A. Operation of a MOEMS deformable mirror in cryo: challenges and results. Micromachines 2017;8(8):233. https://doi.org/10.3390/mi8080233. http://www.mdpi.com/2072-666X/8/8/233.

[22] Takeda M, Ina H, Kobayashi S. Fourier-transform method of fringe-pattern analysis for computer-based topography and interferometry. J Opt Soc Am 1982;72(1):156. https://doi.org/10.1364/JOSA.72.000156. https://opg.optica.org/abstract.cfm?URI=josa-72-1-156.

[23] Bellanger C, Toulon B, Primot J, Lombard L, Bourderionnet J, Brignon A. Collective phase measurement of an array of fiber lasers by quadri-wave lateral shearing interferometry for coherent beam combining. Opt Lett 2010;35(23):3931. https://doi.org/10.1364/OL.35.003931. https://opg.optica.org/abstract.cfm?URI=ol-35-23-3931.

[24] Antier M, Bourderionnet J, Larat C, Lallier E, Lenormand E, Primot J, et al. kHz closed loop interferometric technique for coherent fiber beam combining. IEEE J Sel Top Quantum Electron 2014;20(5):182–7. https://doi.org/10.1109/JSTQE.2014.2302444. http://ieeexplore.ieee.org/document/6722895/.

[25] Penrose R. A generalized inverse for matrices. Math Proc Camb Philos Soc 1955;51(3):406–13. https://doi.org/10.1017/S0305004100030401. https://www.cambridge.org/core/product/identifier/S0305004100030401/type/journal_article.

[26] Deprez M. Moyen de métrologie pour la conception et l'évaluation de chaines lasers hyper intenses utilisant la recombinaison cohérente de lasers élémentaires. Ph.D. thesis. Université Paris-Saclay; 2021.

[27] Rouzé B, Fsaifes I, Bellanger S, Veinhard M, Rousseaux T, Primot J, et al. Phase noise measurements and diagnoses of a large array of fiber lasers by PISTIL. Appl Opt 2022;61(27):7846. https://doi.org/10.1364/AO.466021. https://opg.optica.org/abstract.cfm?URI=ao-61-27-7846.